Trajectory optimization for intra-operative nuclear tomographic imaging

Jakob Vogel [a,1], Tobias Lasser [a,b,*,1], José Gardiazabal [a], Nassir Navab [a]

[a] Computer Aided Medical Procedures (CAMP), Technische Universität München, Boltzmannstraße 3, 85748 Garching b. München, Germany
[b] Institute of Biomathematics and Biometry, Helmholtz Zentrum München, Ingolstädter Landstraße 1, 85764 Neuherberg, Germany

ARTICLE INFO

ABSTRACT

Diagnostic nuclear imaging modalities like SPECT typically employ gantries to ensure a densely sampled geometry of detectors in order to keep the inverse problem of tomographic reconstruction as well-posed as possible. In an intra-operative setting with mobile freehand detectors the situation changes significantly, and having an optimal detector trajectory during acquisition becomes critical. In this paper we propose an incremental optimization method based on the numerical condition of the system matrix of the underlying iterative reconstruction method to calculate optimal detector positions during acquisition in real-time. The performance of this approach is evaluated using simulations. A first experiment on a phantom using a robot-controlled intra-operative SPECT-like setup demonstrates the feasibility of the approach.

1. Introduction

The recent decades have seen tremendous developments in the field of medical imaging, particularly in terms of three-dimensional modalities like CT, MRI, PET or SPECT. However, most of these techniques have mainly been used for diagnostic, pre-operative purposes, despite the valuable nature of intra-operative accurate and patient-specific volumetric imagery. This is due to the massive size, shape and cost of the scanning gantries of diagnostic tomographic devices (as well as imaging time requirements in case of nuclear imaging) and the consequent incompatibility with the operating room workflow.

Imaging technology has significantly advanced in this respect, and intra-operative imaging techniques such as 3D ultrasound and C-arm CT have been applied in clinical practice with success, see for example Fenster and Downey (2000) and Ganguly et al. (2011).

Another recent example of an intra-operative imaging technique is called "Freehand SPECT" (or short: fhSPECT) as introduced in Wendler et al. (2007) with a first clinical setup in Wendler et al. (2010). As in regular SPECT, a radioactive tracer is injected into the patient's body, eventually yielding radioactive hotspots in the marked target tissue (for example cancer cells). The tomographic reconstruction of the activity distribution allows the intra-operative identification and localization of such hotspots. The fhSPECT technique has found clinical application in sentinel node biopsy for breast cancer (Schnelzer et al., 2012), for melanoma (Rieger et al., 2011; Naji et al., 2011), and for oral cancer (Heuveling et al., 2012) as well as in parathyroidectomy (Rahbar et al., 2012). In sentinel node biopsy, the typical patient is injected with a radioactive tracer a few hours before the procedure and a planar scintigraphy is taken to ascertain the tracer uptake. During the biopsy procedure (see Fig. 1a), fhSPECT three-dimensional imaging is used to plan and guide the resection for that particular patient and control any residual radioactivity intra-operatively.

A fhSPECT system consists of a hand-held gamma detector and an optical tracking system for localization of the sensor (see Fig. 1b for an illustration). The measured activity counts and recorded poses can be used to reconstruct the activity map, where the entire process is subject to the same requirements as in usual SPECT: statistically significant counts of radio-active events, and sufficiently many intersecting perspectives covering the region of interest. In case of classical SPECT scanners, the second requirement is guaranteed by design, that is the shape and arrangement of detectors, but in case of freehand-guided detectors as in fhSPECT, the number of perspectives and thus the quality of the process depends heavily on the experience of the operator performing the acquisition scan. To alleviate this, a commercial implementation of fhSPECT, the declipseSPECT system (SurgicEye GmbH, Germany), offers a supporting augmented reality visualization based on a column sum metric to guide the operator. While this visual guidance improves results significantly over no guidance (Wendler et al., 2010), an experienced operator is still required for clinically useful reconstructions. In particular for non-uniform detector trajectories in more complicated cases, this visual guidance scheme is insufficient.

---

* Corresponding author at: Computer Aided Medical Procedures (CAMP), Technische Universität München, Boltzmannstraße 3, 85748 Garching b. München, Germany.

E-mail address: lasser@in.tum.de (T. Lasser).

[1] These authors contributed equally to this work.
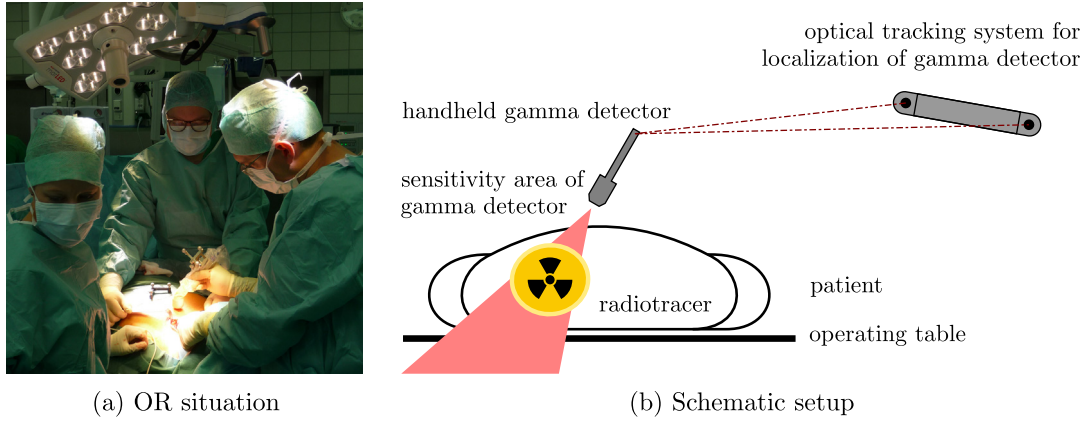
(a) OR situation　　　　　　　　(b) Schematic setup

Fig. 1. (a) Typical setting in the operating room and (b) schematic setup of fhSPECT.

It is thus highly desirable to optimize the scanning trajectories, and to replace the hand-held detector movement with an automated process in order to improve reliability and reproducibility while minimizing the acquisition time. Ideally this trajectory optimization would be performed pre-operatively based on diagnostic three-dimensional imaging data. However, in all typical application scenarios of fhSPECT such three-dimensional pre-operative data is not available, and planning is done only in the operating room itself. Hence the optimization scheme should be incremental and real-time, supporting the patient- and process-specific nature of fhSPECT.

In this work we present energy measures for this purpose based on a tight link to the underlying mathematical principles of algebraic tomographic reconstruction, and based on this energy measure, we suggest an incremental real-time optimization scheme for generating acquisition trajectories. We demonstrate the feasibility of this approach in numerical simulations as well as in an actual experiment for the case of nuclear imaging with a fhSPECT-like setup using a robotic arm.

2. Methods

2.1. Algebraic reconstruction

In tomographic reconstruction we aim to recover a *signal* $f : \Omega \to \mathbb{R}$, where Ω describes a *region of interest* $\Omega \subset \mathbb{R}^3$. In algebraic reconstruction (also referred to as series expansion method or iterative reconstruction), this signal is discretized from the very start:

$$f(\cdot) \approx \hat{f}(\cdot) = \sum_i x_i b_i(\cdot), \tag{1}$$

where $b_i : \Omega \to \mathbb{R}$ denotes a set of suitable *basis functions*, for example a voxel grid. The *coefficient vector* $\mathbf{x} := (x_i)$ is initially unknown, and the algebraic reconstruction problem is exactly the recovery of it.

This is done by linking the signal with the measurement geometry and detector values through linear *measurement models* $\mathcal{M}_j : (\Omega \to \mathbb{R}) \to \mathbb{R}$, including all geometric information and encoding the entire physical process leading from the signal f to a certain *measurement* m_j as $\mathcal{M}_j(f) = m_j$. In X-ray CT for example, a suitable model would be the Radon transform of f.

These models can also be applied to the discretized signal,

$$\mathcal{M}_j \left(\sum_i x_i b_i \right) = m_j,$$

and – using the linearity of $\mathcal{M}_j$ – the equation can be rearranged:

$$m_j = \sum_i x_i \underbrace{\mathcal{M}_j(b_i)}_{=:a_{ji}}.$$

This linear sum has the same coefficients (x_i) as sought before, and the second factor contains the measurement models applied to the basis functions. For a single measurement j and all basis functions (with running index i), the latter can be collected into a row vector $\mathbf{a}_j = (a_{ji})$, such that

$$m_j = \left\langle \mathbf{a}_j^T, \mathbf{x} \right\rangle.$$

Repeating the process for each measurement, it is possible to obtain a system of linear equations:

$$\mathbf{m} := \begin{pmatrix} m_1 \\ m_2 \\ \vdots \end{pmatrix} = \begin{pmatrix} \langle \mathbf{a}_1^T, \mathbf{x} \rangle \\ \langle \mathbf{a}_2^T, \mathbf{x} \rangle \\ \vdots \end{pmatrix} = \underbrace{\begin{pmatrix} -\mathbf{a}_1- \\ -\mathbf{a}_2- \\ \vdots \end{pmatrix}}_{=:A} \mathbf{x}. \tag{2}$$

This linear system can then be solved either by using standard techniques such as the conjugate gradient method (CG) or the algebraic reconstruction technique (ART), or by statistical algorithms such as MLEM, for an overview see Herman (2010). The solution vector $\mathbf{x}$ is afterwards converted into an approximation of the desired signal f by inserting it into its discretization formula (1).

Note that the *system matrix* $A = (\mathbf{a}_j)$ contains all relevant geometrical information with one row corresponding to one measurement, while the actual measured values from the detector are stored independently in the right-hand side vector $\mathbf{m}$.

In the case of fhSPECT, f is the distribution of the radioactive tracer. As basis functions b_i we use a regular voxel grid, while $\mathcal{M}_j$ is implemented as an analytical approximation of the cone-shaped sensitivity response function of the hand-held gamma detector, as detailed by Lasser et al. (2011). During intra-operative acquisition of data by moving the hand-held detector over the patient, the system matrix A is computed incrementally row by row, enabling our proposed incremental, real-time trajectory optimization scheme.

2.2. Evaluating geometries with energy measures

The measurement poses used to construct the linear system (2) are either defined by the fixed design of the scanning gantry, or are determined by the (more or less intentional) trajectory chosen by a human guiding the hand-held detector. An obvious approach for assessing the geometry would be to directly relate the basis functions and measurement rays/poses. However, these entities have already been considered while setting up the linear system, and

are thus available in an abstract and more general sense within the system matrix A. It is thus sufficient to consider this matrix and its properties such as condition and rank, as one would do for other arbitrary linear systems.

In the following we are suggesting scalar-valued energy measures based on such properties, to enable comparison of detector trajectories.

2.2.1. Column Sums of A

Let $\mathbf{c}_i = (a_{ji})$ denote the ith column vector of the system matrix A,

$$A = \begin{pmatrix} | & | & \\ \mathbf{c}_1 & \mathbf{c}_2 & \cdots \\ | & | & \end{pmatrix}.$$

Each column vector $\mathbf{c}_i$ then contains the impacts of all measurements onto the basis function b_i. $\mathbf{c}_i = \mathbf{0}$ implies that no measurement hit this basis function, while a high accumulated sum $\hat{c}_i = \sum_j a_{ji}$ implies good coverage.

In the commercial system declipseSPECT (SurgicEye GmbH, Germany), the $\hat{c}_i$ are shown as a volume rendering in an augmented reality view for operator guidance, see also Wendler et al. (2010).

In order to optimize a detector trajectory, we propose to use the ℓ_1-norm of the coverage vector $\hat{\mathbf{c}} = (\hat{c}_i)$ as an energy measure:

$$\eta_C(A) := \|\hat{\mathbf{c}}\|_{\ell_1} = \sum_i \hat{c}_i = \sum_{i,j} a_{ji}. \tag{3}$$

Maximizing this measure η_C should thus yield a better measurement coverage of the region of interest Ω.

2.2.2. Null-space estimation of A

Assuming a null-space vector $\tilde{\mathbf{x}}$, that is $A\tilde{\mathbf{x}} = \mathbf{0}$, and a vector $\mathbf{x}$ solving $A\mathbf{x} = \mathbf{m}$, an additional solution vector can be trivially computed: $A(\mathbf{x} + \tilde{\mathbf{x}}) = \mathbf{m}$. This leads to ambiguity, and a good trajectory will aim to reduce A's kernel to the vector $\mathbf{0}$, see Zeng and Gullberg (2011).

To estimate the null-space of A, we calculate approximate solutions $\tilde{\mathbf{x}}_k$ to $A\tilde{\mathbf{x}} = \mathbf{0}$ using 20 iterations of the conjugate gradient method for k different random, non-zero initial values. $\|\tilde{\mathbf{x}}_k - \mathbf{0}\|_{\ell_2}$ should then be minimal in order for the kernel of A to be close to $\mathbf{0}$.

For trajectory optimization we thus define the energy measure

$$\eta_N(A) := -\max_k \|\tilde{\mathbf{x}}_k\|_{\ell_2}. \tag{4}$$

This energy will be higher for measurement configurations with less ambiguity. However, each evaluation of this energy measure is relatively costly, as it involves solving several linear systems iteratively.

2.2.3. Singular values

The system matrix A can be decomposed as

$$A = U \underbrace{\begin{pmatrix} \sigma_1 & & \\ & \sigma_2 & \\ & & \ddots \end{pmatrix}}_{=:D} V^T$$

using singular value decomposition (SVD). The typical singular value spectrum of a system matrix (see Fig. 2a) will show some large values with low indices, and some very low values with high indices. Even for badly conditioned matrices (caused by sub-optimal trajectories), however, there will not be a true rank deficiency, and no clear threshold to distinguish relevant from irrelevant singular values. Matrices with good condition, on the other hand, will show a very similar spectrum, only with a steeper slope.

Consequently, an energy measure needs to consider the entire spectrum, thus we propose

$$\eta_S(A) := \sum_i \sigma_i = \|\mathrm{diag}(D)\|_{\ell_1}. \tag{5}$$

This energy value will yield higher values for better-conditioned system matrices, however, it is only useful for comparing matrices of the same size. As the number of columns equals the number of basis functions chosen (which is usually fixed beforehand), this constraint relates particularly to the number of rows; that is, the number of measurements must be equal for the two matrices to be compared.

Furthermore, computing the SVD is very slow due to its iterative computation. However, as suggested by Gu and Eisenstat (1994) and extended by Chetverikov and Axt (2010) and Vogel et al. (2012), the SVD can be computed using an incremental scheme, matching the incremental nature of collecting data while moving the detector.

2.2.4. Pivoted QR

Though the most famous, the SVD is only one member out of the set of rank-revealing decompositions. Another, considerably faster one is the pivoted QR decomposition

$$A = Q \underbrace{\begin{pmatrix} r_{11} & r_{12} & \cdots \\ & r_{22} & \cdots \\ & & \ddots \end{pmatrix}}_{=:R} P^T,$$

where Q is orthogonal and P a permutation matrix (and thus also orthogonal). Not only is the structure of this decomposition very similar to the SVD's, the spectra $\mathrm{diag}(D)$ and $\mathrm{diag}(R)$ are also correlated (see Fig. 2). A detailed description of this correlation is given by Fierro and Hansen (1995).

The cost function can thus be adapted to

$$\eta_Q(A) := \sum_i |r_{ii}| = \|\mathrm{diag}(R)\|_{\ell_1} \tag{6}$$

and a very similar behavior in comparison to the SVD-based measure η_S can be expected (see Fig. 3 for the energy evolution of random paths). In contrast to SVD, however, the computation is non-iterative and thus considerably faster.

2.3. Trajectory optimization

For incremental real-time optimization of the trajectory, we use the time required for the detector to move from a previous position to the current location $\mathbf{p}_j$ to calculate the next best destination $\mathbf{p}_{j+1}$ (see Fig. 4).

In more detail: a surface model $\mathcal{S}$ of the patient (stored as a triangle mesh) is used to describe the permissible region where the detector tip may be located. This model should include reachability limitations as posed by the particular operating room scenario.

While the detector is moving to location $\mathbf{p}_j \in \mathcal{S}$ corresponding to measurement j, the system matrix A_j containing the known measurement poses from $\mathbf{p}_1$ to $\mathbf{p}_j$ is computed. To find the next best destination $\mathbf{p}_{j+1}$ of the trajectory, candidate poses $\mathbf{p}_* \in \mathcal{S}$ on the surface model are evaluated by adding the corresponding system matrix row $\mathbf{a}_*$ to A_j and computing

$$\eta \begin{pmatrix} A_j \\ \mathbf{a}_* \end{pmatrix}$$

for one of the energy measures η. Doing this for all triangles yields a 'measurement priority' for the entire surface model (see Fig. 5).

Note that the theoretical problem of finding the most orthogonal sensor perspective is computationally not feasible, but can be
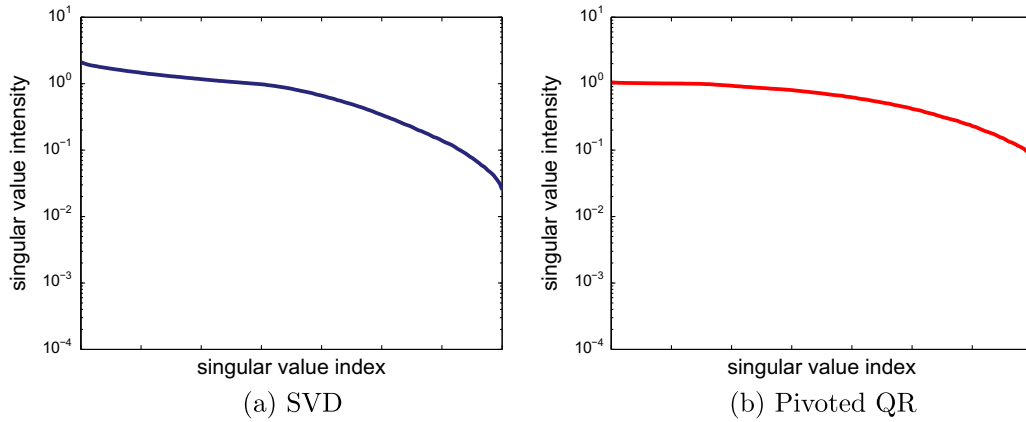
Fig. 2. Two spectra, the first showing the singular values σ_i (blue), and the second the pseudo-singular values $|r_{ii}|$ from Pivoted QR (red). (For interpretation of the references to color in this figure legend, the reader is referred to the web version of this article.)
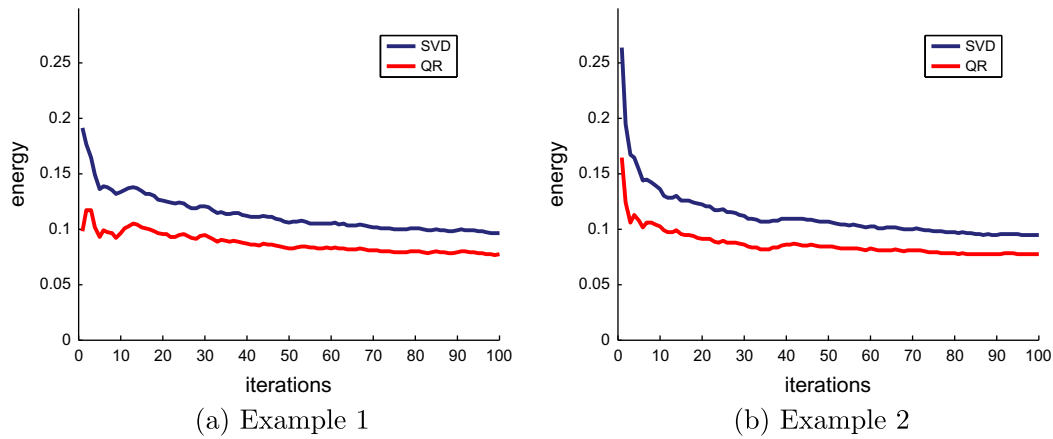

Fig. 3. Evolution of the SVD- (blue) and QR-based (red) energies η_S and η_Q for two random trajectories. The horizontal axis shows the number of measurements used for setting up the system matrix, that is the number of system matrix rows. The vertical axis denotes the energy value. From a certain, small number of poses onwards, the two curves behave very similarly and run almost in parallel. (For interpretation of the references to color in this figure legend, the reader is referred to the web version of this article.)

approximated well using random sampling (Strohmer and Vershynin, 2006). Therefore, we visit each triangle of the bounding mesh and generate a random pose $\mathbf{p}_*$ within its boundary. The triangle yielding the optimal cost (that is, the highest priority for measurement) is stored, and the respective random pose is taken as the next destination $\mathbf{p}_{j+1} := \mathbf{p}_*$.

Apart from optimizing one of the cost functions η, it is also possible to impose additional constraints, such as a certain minimal step length or reachability on the surface model $\mathcal{S}$ from $\mathbf{p}_j$. This is done by excluding poses violating one of these conditions from the optimization process. For this work we use a minimal step length of 50 mm and assume that each position on the triangle mesh is reachable.

As soon as the detector has reached the current destination $\mathbf{p}_j$ and a sufficiently substantiated next destination $\mathbf{p}_{j+1}$ has been found, the per-triangle-costs and random poses are cleared, and the process starts again.

Very importantly, this evaluation can be performed for several candidate poses in parallel and can thus be accelerated linearly by adding additional computing nodes. When visiting the triangles in a randomized order, we can also expect to obtain a significant distribution of the 'measurement priority' long before all triangles have been processed, and an early abort is possible, greedily choosing the best known candidate so far. In this work we enforce a minimal triangle 'sampling rate' of 15% before we allow the trajectory to continue.

Note that we do not consider the paths between $\mathbf{p}_j$ and the random poses $\mathbf{p}_*$ while optimizing. This is necessary for the spectrum-based energy measures, as they can only compare matrices of the same size. As soon as the next destination is fixed, however, measurements are acquired continuously while moving towards it.
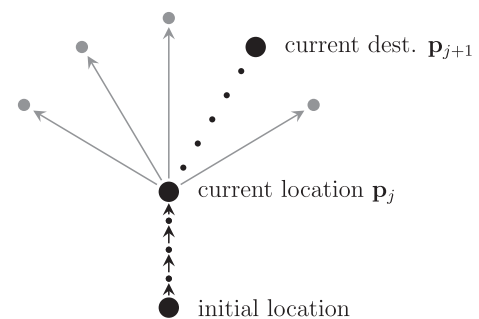

Fig. 4. Schematic view. While moving from the initial to the current location, the optimization scheme tests several candidates (gray). As soon as a new destination must be picked, the best currently computed candidate is chosen. Ideally, the sampling of candidates is complete at that time, but using randomized testing allows early termination.
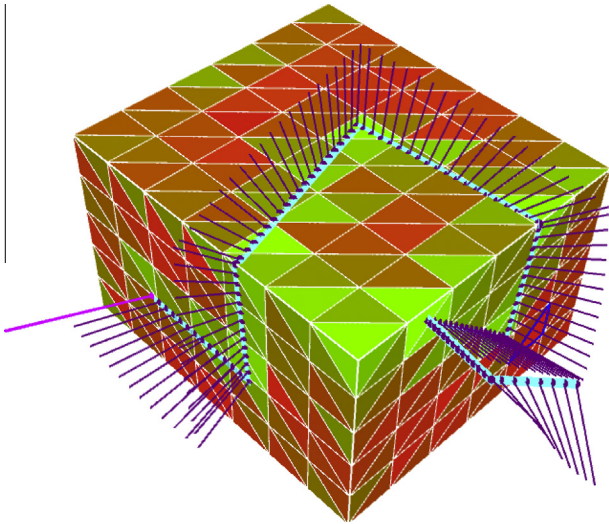
Fig. 5. Screenshot of the actual trajectory optimization program. The triangulated bounding box consists of regions where measurements should be collected (red and green). Red triangles denote planes that should be visited while sufficient measurements are already available for the green triangles; the color is directly computed from the energy η. Note that the traversed path (cyan, with purple measurement poses) correlates to green triangles. (For interpretation of the references to color in this figure legend, the reader is referred to the web version of this article.)

3. Experiments and results

In order to test the proposed approach, we have implemented the proposed optimization framework on a 2.3 GHz Intel Core i7 quad-core portable computer with 8 GB of RAM using Boost threads for parallelization.

Besides parallelization, we compute the candidate poses using a downsampled voxel grid ($10 \times 10 \times 7$), we visit the triangles in random order, and use early abort if time runs out and at least 15% of the triangles have been evaluated. Our implementation is thus able to generate positions in real-time for all measures (except η_N, see below), i.e. it can provide measurement poses often enough for the detector to keep moving until sufficient measurements have been acquired. A typical computed trajectory in an early stage of the optimization is shown in Fig. 5.

We evaluated the optimization scheme and the energy measures η_C, η_N, η_Q in numerical simulations. Using the best energy measure η_Q we also performed a first real experiment in a fhSPECT-like setup, where a robotic arm is executing the optimized trajectory.

3.1. Trajectories

We performed several experiments where we compare trajectories of different nature. In all cases, we measured three adjacent sides of a bounding box of size $120 \times 120 \times 87$ mm, thus simulating the perspectives available during a typical procedure employing fhSPECT (sentinel node biopsy for breast). The generated paths can be categorized as follows:

- *Spectrum trajectories* (Fig. 6a) have been generated using the control scheme presented in this article, and attempt to optimize the QR-based measure η_Q. For the simulation experiments, such paths have been recorded to disk with a smooth interpolation between positions $\mathbf{p}_j$.
- *Column-sums and null-space trajectories* have been computed similarly, but instead optimizing the column sum measure η_C and the null-space measure η_N, respectively.

- *Random trajectories* (Fig. 6b) have been created by smoothly connecting random poses in random triangles. The same smooth interpolation as above has been used for connecting these poses.
- *Human trajectories* (Fig. 6c) have been recorded by a human expert operator in reality using an optical tracking system, and have later been re-mapped to fit the surface model. The path has been enhanced further by moving the detector as close as possible to the surface model, and by using a smooth interpolation method to guarantee good coverage. This makes the human path directly comparable to the other trajectories.
- *Grid or structured pattern trajectories* (Fig. 6d) follow a simple regular motion pattern uniformly distributed on the surface, with the detector orthogonal to the bounding box. This seeks to simulate the motion pattern of inexperienced operators.

Each trajectory was generated to contain about 2000 measurements, corresponding to a clinically acceptable scanning time of 3–5 min. For the optimized and random trajectories, we generated 10 randomized trajectories per class and consider the mean behavior with standard deviations in plots and when giving numbers.

3.2. Evolution of optimized energy

First, we assume for the moment that our rank-motivated energy measure η_Q really prefers better-posed reconstruction problems and that such linear systems yield better reconstructions. We hence checked whether the optimization scheme really results in better numerical condition of the system matrix and compared the evolution of our energy values η_Q with increasing path length for the sample trajectories, as shown in Fig. 7.

The optimization scheme using η_Q (called spectrum) indeed yields the largest condition estimates for the linear problems set up from the respective trajectories, as can be expected by design of the method. More importantly, the level of the spectrum-optimized energies, including standard deviation, is considerably higher than the level of the other approaches. Only the null-space based measure is also performing better than chance level, while the more structured (among them a human expert) and state-of-the-art methods (column sums) perform below the random trajectories.

3.3. Numerical simulations

Next, we checked the assumption of better reconstruction results guaranteed by higher system matrix condition, using a simulated setting. Consequently, we have generated numerical phantoms showing different configurations of spherical activity hotspots, and we used the forward acquisition model to simulate measurements. We neither added noise, nor did we attempt to model nuclear statistics, in order to focus on purely trajectory-related influences on the convergence of the image reconstruction process.

Using such virtual acquisitions for the different settings, we generated reconstructions for increasing numbers of measurements, up to about 2000. The reconstructions were performed on a $71 \times 71 \times 50$ voxel grid (voxel size 1.4 mm^3), using 80 iterations of ART with a relaxation factor of 0.1. The major difference to a real measurement – apart from nuclear statistics – is that data is only simulated at control points, and not continuously at a certain sampling rate while moving the detector.

In the resulting reconstructions, we compared the centers of gravity of all reconstructed activity hotspots with their respective ground truth locations. The centers of gravity were extracted from the reconstruction results by starting at the ground truth location and walking uphill towards a local intensity maximum. This iden-
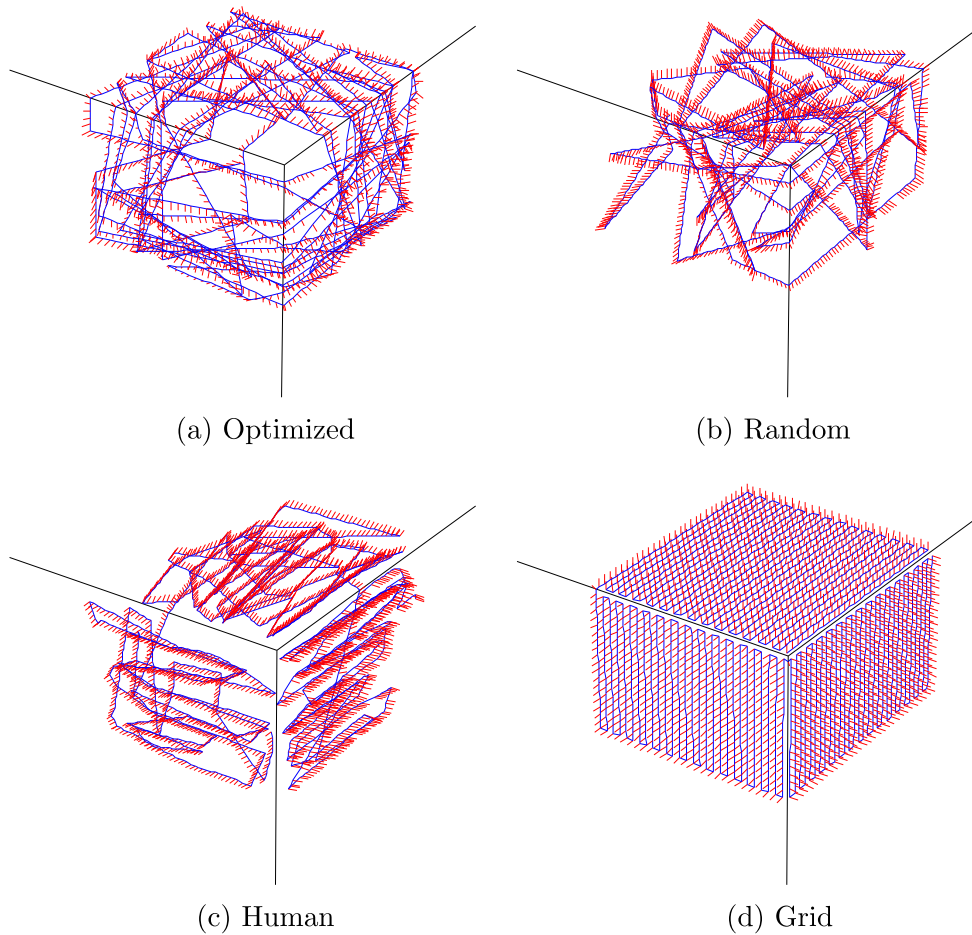
J. Vogel et al./Medical Image Analysis 17 (2013) 723–731

(a) Optimized

(b) Random

(c) Human

(d) Grid

Fig. 6. Sample trajectories (blue) with orientations (red). The black lines are the edges of the bounding box. The vertical axis is the *Z* axis, the horizontal plane is the *X/Y*-plane. Note that the optimized path has few clusters and good coverage. At first glance the grid path shares this property, but there are many complementary poses with only three viewing directions in total. (For interpretation of the references to color in this figure legend, the reader is referred to the web version of this article.)
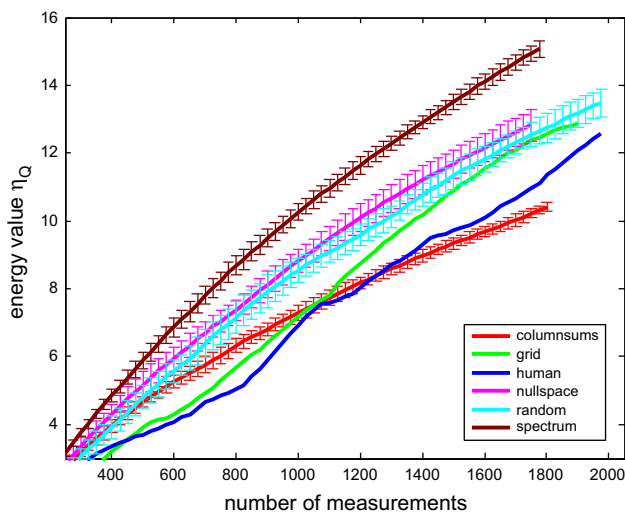

Fig. 7. Energies η_Q (vertical axis) over trajectory length (horizontal axis). Apart from the "grid" and "human" paths, where only single typical examples are shown, we have computed 10 (randomized) examples per class and show the mean curves with standard deviation. It is not surprising that more measurements (thus more system matrix rows) lead to larger energies, the decisive property is thus growth of the curve and its relative magnitude. Here, the spectrum-based measure (maroon) clearly features fastest growth and highest value, thus yielding optimal condition for the linear problem solved during reconstruction. (For interpretation of the references to color in this figure legend, the reader is referred to the web version of this article.)

tification method is justified as intra-operative nuclear reconstructions typically show rather simple structures with (almost convex) activity hotspots, where higher activity is usually reconstructed at the centers of the active regions. In particular, this process is more robust than sphere matching or blob identification, as it does not depend on thresholding parameters.

Fig. 8 shows the result of such an experiment with a particularly difficult configuration. There, we simulated two spherical activity hotspots with different radii (7 mm and 14 mm), located closely next to each other (21 mm separation). In this setting, only good trajectories yield a result where the two hotspots are distinguishable. In fact, for the column sum based trajectories as well as the human and grid trajectories, a separation of the hotspots was not possible. Conversely, starting at around 1000 measurements, the spectrum and null-space based as well as the random trajectories allow separation of the hotspots. The lowest mean error with lowest variance is shown by the spectrum based method.

3.4. Actual measurements

To confirm our simulation results, we performed a first real experiment in a fhSPECT-like setup using a phantom with radioactive spheres and a robotic arm for detector movement.

A gamma detector (Crystal Photonics, Berlin, Germany) is mounted to the wrist of an UR5 robotic arm (Universal Robots, Odense, Denmark), as shown in Fig. 9. In addition to the coordinate frames obtained via forward kinematics, we use transformations
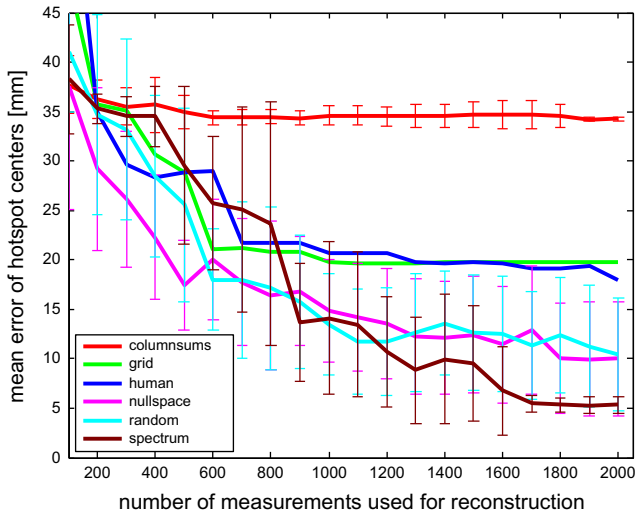
Fig. 8. Behavior of error with increasing number of measurements. The vertical axis shows the mean error magnitude between the ground-truth and reconstructed centers of all activity hotspots in mm; the horizontal axis denotes the number of measurements being used for reconstruction. Apart from the "grid" and "human" paths, where only single typical examples are shown, we have computed 10 (randomized) examples per class and show the mean curves with standard deviation. Using several hundred measurements, all methods yield reconstruction results, however, the smallest error values (with small standard deviation) are obtained from the proposed spectrum-optimized paths (maroon). (For interpretation of the references to color in this figure legend, the reader is referred to the web version of this article.)

provided by a Polaris Vicra optical tracking system (Northern Digital, Waterloo, Canada) for calibration and localization of the phantom.

We are imaging a box phantom (see Fig. 10) containing three hollow spheres (diameter 9.86 mm) filled with a ^{99m}Tc solution with an activity of 1 MBq arranged in a triangular fashion. The trajectory optimization software used a simple triangulated surface model of the box, accessible from three sides and used the spectrum based measure η_Q to generate 1665 measurement positions. The robot is fed with those measurement positions directly and moves to these position based on inverse kinematics calculations using the triangulated surface model of the box for collision detection. The resulting data is reconstructed on a $120 \times 120 \times 60$ voxel grid (voxel size 1.25 mm^3) using 60 MLEM iterations.
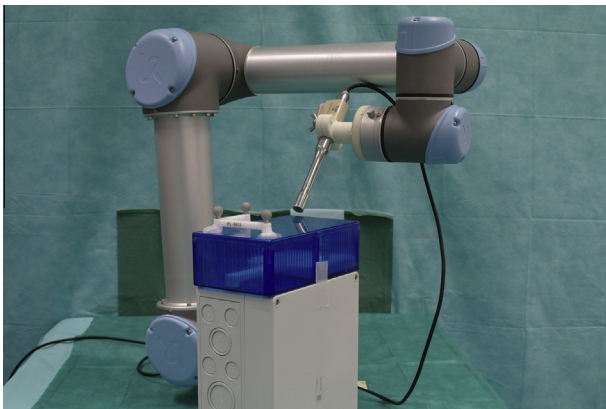

Fig. 9. Robotic arm with gamma detector attached to wrist. Also visible are a blue box phantom containing radioactive spheres, as well as retro-reflective marker spheres for the infrared tracking system. (For interpretation of the references to color in this figure legend, the reader is referred to the web version of this article.)

A central slice of the 3D reconstruction is shown in Fig. 10. The locations of the three hotspots are recovered with reasonable accuracy, considering that the reconstruction problem is massively underdetermined (system matrix $A \in \mathbb{R}^{1,665 \times 864,000}$). A separation of the two closer hotspots, which are separated by 15 mm, was not possible.

4. Discussion

The singular value decomposition of the system matrix A is a common tool to study imaging geometries (Lasser and Ntziachristos, 2007). As the singular value decomposition is costly to compute, even with incremental computing schemes (Vogel et al., 2012), we proposed using another fast, rank-revealing decomposition in this work, the pivoted QR decomposition. The diagonal entries of the R matrix are correlated with the singular values of A and hence also allow an evaluation of the imaging geometry. Based on this finding we suggested an energy measure η_Q (also called 'spectrum-based') to evaluate detector trajectories for use in a randomized optimization scheme.

The randomized optimization scheme was also applied to other energy measures: a mathematically motivated null-space based measure η_N, and a column-sum based measure η_C adapted from the commercial declipseSPECT system. The resulting trajectories were compared to random trajectories as well as a structured, uniformly distributed grid trajectory and a trajectory from a human expert.

The column-sum based trajectories allow for consistent results with low standard deviation in the 10 trial runs, but cannot improve results over a human expert or a structured grid trajectory, both of which show comparable performances. As high column sum values can also be achieved by complementary poses instead of intersecting views, this leads to a worse performance in comparison to a human expert or grid trajectory, which contain more intersecting views. This also fits in with clinical experience, where human experts typically acquire better images than operators relying purely on the column-sum guidance of the declipseSPECT system.

Random trajectories show high variations, but in the mean perform better than the human expert or the structured grid trajectory. The null-space trajectories finally employs optimization based on the system matrix condition via kernel estimation and shows good results particularly in the region of up to 800 measurements. After that, its performance levels off. This is due to its computational complexity, which means that as the system matrix size increases, the optimization algorithm is no longer able to visit most of the triangles and starts hitting the minimal triangle testing rate of 15%. In fact, the average triangle sampling rate of the null-space method is 20% over all measurement poses on our testing hardware, while the column-sum and spectrum based methods achieve 85% on average. The null-space method actually violates the real-time requirement occasionally due to having to sample at least 15% of the triangles.

Finally, the spectrum based trajectories show the best performance with very low deviations, particularly for higher measurement numbers of 1700 and onwards. This behavior is perfectly acceptable, as clinical data sets typically feature 2000–3000 measurements, corresponding to scanning times of 3–5 min.

The proposed optimization scheme computes detector positions. These poses can then be automatically executed for example by a robotic arm. The feasibility of this approach was shown with a first real phantom experiment, where a fhSPECT-like setup with a robotic arm holding the detector executed the spectrum-based optimized trajectory.
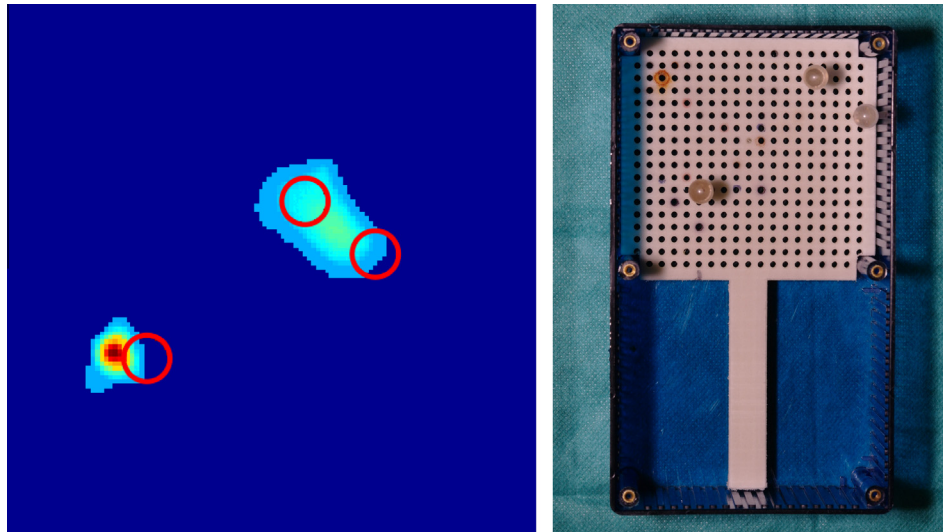
Fig. 10. Central slice (left) of the 3D reconstruction of the radioactivity distribution in the box phantom containing three hollow spheres filled with a ^{99m}Tc solution (right). The ground truth positions of the spheres are marked by circles in red. (For interpretation of the references to color in this figure legend, the reader is referred to the web version of this article.)

Adding a robotic device to the surgical theater is naturally a complex undertaking. Besides additional cost, taking up extra space and adding additional points of failure, various safety issues need to be taken care of. A simpler approach might be to project the computed trajectory positions directly onto the patient using a steerable laser pointer, or to use an augmented reality visualization. While this still includes the human factor and will yield less reproducible results, the incremental, real-time nature of the optimization scheme will be able to adapt to any deviations of the human operator while performing the computed trajectory.

The optimization scheme requires a surface model of the patient to select the measurement poses. For the experiments in this work the object to be scanned was a box phantom, allowing us to use a simple triangulated bounding box. In a clinical setting, the bounding surface would have to be acquired for example from segmented pre-operative data or a laser-scanned model. It would even be possible to have the surgeon define a rough bounding box on-the-fly using a tracked pointing device directly on the patient, but this would give up the added detection sensitivity of having the detector as close to the surface as possible. Reachability constraints also have to be incorporated into this surface model.

While the optimization scheme was inspired by fhSPECT, our approach only relies on principles and concepts used in general tomographic reconstruction, and is thus not limited to the fhSPECT modality. Using different measurement models $\mathcal{M}_j$, the approach is also directly applicable to other tomographic modalities, like for example robotic C-arm CT. Used in an offline fashion, it would also be possible to optimize scanner designs.

Finally, our approach currently only takes into account the patient-specific surface model to optimize the detector geometry. It is also conceivable to add information from the actual detector measurements into the cost-function. This, however, adds the risk of adding bias into the reconstructions and potentially missing critical hotspots completely. Hence this extension would also require corresponding, registered pre-operative imaging data to ensure correct reconstructions.

5. Conclusion

We have presented energy measures directly linking the trajectory for data acquisition with the underlying reconstruction problem. Furthermore, we have shown an incremental scheme optimizing these target functions capable of running in real-time.

Numerical experiments have shown the feasibility and the potential of the proposed method, with the best results being generated using the spectrum based energy measure. A first real experiment using a robotic arm has confirmed the simulation results.

References

Chetverikov, D., Axt, A., 2010. Approximation-free running SVD and its application to motion detection. Pattern Recognition Letters 31, 891–897.

Fenster, A., Downey, D.B., 2000. Three-dimensional ultrasound imaging. Annual Review of Biomedical Engineering 2, 457–475.

Fierro, R.D., Hansen, P.C., 1995. Accuracy of TSVD solutions computed from rank-revealing decompositions. Numerische Mathematik 70, 453–471.

Ganguly, A., Fieselmann, A., Marks, M., Rosenberg, J., Boese, J., Deuerling-Zheng, Y., Straka, M., Zaharchuck, G., Bammer, R., Fahrig, R., 2011. Cerebral CT perfusion using an interventional C-arm imaging system: cerebral blood flow measurements. American Journal of Neuroradiology 32, 1525–1531.

Gu, M., Eisenstat, S.C., 1994. A Stable and Fast Algorithm for Updating the Singular Value Decomposition. Research Report RR-966, Yale University, New Haven.

Herman, G.T., 2010. Fundamentals of Computerized Tomography, second ed. Springer, London.

Heuveling, D., Karagozoglu, K., van Schie, A., van Weert, S., van Lingen, A., de Bree, R., 2012. Sentinel node biopsy using 3D lymphatic mapping by freehand SPECT in early stage oral cancer: a new technique. Clinical Otolaryngology 37, 89–90.

Lasser, T., Ntziachristos, V., 2007. Optimization of 360° projection fluorescence molecular tomography. Medical Image Analysis 11, 389–399.

Lasser, T., Ziegler, S.I., Navab, N., 2011. Freehand SPECT in low uptake situations. In: Proc. of SPIE 7961, p. 79611Z.

Naji, S., Tadros, A., Traub, J., Healy, C., 2011. Case report: improving the speed and accuracy of melanoma sentinel node biopsy with 3D intra-operative imaging. Journal of Plastic, Reconstructive and Aesthetic Surgery 64, 1712–1715.

Rahbar, K., Colombo-Benkmann, M., Haane, C., Wenning, C., Vrachimis, A., Weckesser, M., Schobar, O., 2012. Intraoperative 3-D mapping of parathyroid adenoma using freehand SPECT. EJNMMI Research 2, 51.

Rieger, A., Saeckl, J., Belloni, B., Hein, R., Okur, A., Scheidhauer, K., Wendler, T., Traub, J., Friess, H., Martignoni, M., 2011. First experiences with navigated radio-guided surgery using freehand SPECT. Case Reports in Oncology 4, 420–425.

Schnelzer, A., Ehlerding, A., Blümel, C., Okur, A., Scheidhauer, K., Paepke, S., Kiechle, M., 2012. Showcase of intraoperative 3D imaging of the sentinel lymph node in a breast cancer patient using the new freehand SPECT technology. Breast Care 7, 484–486.

Strohmer, T., Vershynin, R., 2006. A randomized solver for linear systems with exponential convergence. In: Approximation, Randomization, and Combinatorial Optimization. Algorithms and Techniques. LNCS, vol. 4110. Springer, pp. 499–507.

Vogel, J., Reichl, T., Gardiazabal, J., Navab, N., Lasser, T., 2012. Optimization of acquisition geometry for intra-operative tomographic imaging. In: Medical Image Computing and Computer Assisted Interventions (MICCAI). LNCS, vol. 7512. Springer, pp. 42–49.

Wendler, T., Hartl, A., Lasser, T., Traub, J., Daghighian, F., Ziegler, S., Navab, N., 2007. Towards intra-operative 3D nuclear imaging: reconstruction of 3D radioactive distributions using tracked gamma probes. In: Medical Image Computing and Computer Assisted Interventions (MICCAI), LNCS. vol. 4792. Springer, pp. 252–260.

Wendler, T., Herrmann, K., Schnelzer, A., Lasser, T., Traub, J., Kutter, O., Ehlerding, A., Scheidhauer, K., Schuster, T., Kiechle, M., Schwaiger, M., Navab, N., Ziegler, S., Buck, A., 2010. First demonstration of 3-D lymphatic mapping in breast cancer using freehand SPECT. European Journal of Nuclear Medicine and Molecular Imaging 37, 1452–1461.

Zeng, G.L., Gullberg, G.T., 2011. Null-space function estimation for the three-dimensional interior problem. In: Proc. of Fully 3D, Potsdam. pp. 241–245.